SAND2017-21350C

Calorimetry and Imaging of Plasma Produced by a Pulsed Nanosecond Discharge Igniter in EGR Gases at Engine-Relevant Densities

Author, co-author (Do NOT enter this information. It will be pulled from participant tab in MyTechZone)

Affiliation (Do NOT enter this information. It will be pulled from participant tab in MyTechZone)

Abstract

Pulsed nanosecond discharges (PND) can achieve ignition in internal combustion engines through enhanced reaction kinetics as a result of elevated electron energies without the associated increases in translational gas temperature that cause electrode erosion. Atomic oxygen (O), including its electronically excited states, is thought to be a key species in promoting low-temperature ignition. In this paper, high-voltage (17-24 kV peak) PND are examined in oxygen/nitrogen/carbon dioxide/water mixtures at engine-relevant densities (up to 9.1 kg/m^3) through pressure-rise calorimetry and direct imaging of excited-state O-atom and molecular nitrogen (N_2) in an optically accessible spark calorimeter, with the anode/cathode gap distance set to 5 mm or with an anode-only configuration (DC corona). The conversion efficiency of pulse electrical energy into thermal energy was measured for PND with secondary streamer breakdown (SSB) and similar low-temperature plasmas (LTP) without. The calorimetry measurements confirm that, similar to inductive spark discharges, SSB discharges promote ignition by increasing the local gas temperature. LTP discharges, on the other hand, had very little local gas heating, with electrical-to-thermal energy conversion efficiencies of ~1% at 9 bar. Instead, LTP discharges were found to generate substantial electronically-excited O-atom populations at lower pressures, but the observed image intensity decreased rapidly as the initial pressure was increased. The observed O-atom emission peaked ~20 ns after the start of the pulse and was concentrated near the anode and cathode tips, indicating that the presence of the cathode was beneficial for increasing radical production (although the likelihood of SSB increased). Decreasing oxygen and increasing carbon dioxide concentrations were found to reduce the observed image intensity, but had minimal impact on SSB probability and electrical-to-thermal conversion efficiency. The impact of changes in collisional quenching and the electron energy distribution on image intensity were evaluated.

Introduction

Plasmas — defined here as globally neutral gaseous mixtures of positively- and negatively-charged particles that interact by electric forces in a collective manner — have long been used to control ignition and combustion processes. Conventional inductive coil sparks that feature thermal plasmas with electron energies in equilibrium with the bulk gas energy have fallen out of favor for next-generation automotive engines due to excessive electrode erosion rates from high-temperature arc discharges and poor tolerance to dilution by air or exhaust-gas recirculation (EGR) [1]. Conversely, ignition induced by non-equilibrium low-temperature plasma (LTP), where an imbalance exists between ion and electron temperatures, leads to enhanced reaction kinetics as a result of elevated electron energies without the associated translational gas temperature increases that cause electrode erosion. Automotive low-temperature plasma-assisted ignition (PAI) systems extend dilution tolerance limits through the formation of active radicals that shorten ignition delays [2] and rapid heating via electron energy transfer processes [3-5]. Ignition kernel expansion speeds may also be influenced by hydrodynamic instabilities and ionic winds [6, 7]. LTP generated atomic oxygen (O-atom) in particular, including its electronically-excited states, has been identified as an important radical species that accelerates hydrogen abstraction from the fuel, which in turn increases overall mixture reactivity [8]. For automotive engine combustion, these attributes reduce ignition delay times, suppress knock inducing end-gas auto-ignition, alter fuel reactivity and diffusivity characteristics, and improve noxious emission oxidation [9].

LTP are generally classified by the reduced electric field strength, or the electric field strength (E) normalized by the gas number density (N), in units of Townsend (Td). Broadly speaking, PAI systems sorted by increasing E/N include: microwaves (10 – 50 Td) [3, 10-13], high-frequency resonant discharges (50 – 200 Td) [7, 13-17], and pulsed nanosecond discharges (PND) (100 – 1000 Td) [2, 4, 13, 18-21]. PND igniters typically have electron temperatures above 10 electron volts (eV) using only modest pulse energies (10s of mJ) due to the truncated discharge [22-25]. PND are characterized by higher electron energy, higher peak current, and lower gas temperature compared to both microwave and high-frequency resonant discharges [13]. Since LTP-related ionization and dissociation rates increase with higher E/N due to limited collisional electron energy transfer effects [26], several recent PAI experiments have focused on PND systems [23, 25, 27].

Cathode-directed PND, such as those used in this work, have two discharge phases: the primary streamer and the secondary streamer. The primary streamer propagates as a “plasma bullet” across the electrode gap (O(1 ns)), with intense E/N at the primary streamer head. After the primary streamer reaches the cathode, a slower secondary streamer with lower E/N begins to propagate from the anode. If the secondary streamer reaches the cathode (O(10 ns)), breakdown occurs; this will be referred to as secondary streamer breakdown (SSB) throughout this paper. The likelihood of SSB increases for decreased gas resistance; i.e., from low pressures, high

temperatures, short electrode gap distances, or gases with low ionization potential [28, 29]. A SSB discharge more closely resembles a thermal plasma spark than a LTP discharge with 2 key differences: (1) the electrical-to-thermal energy transfer is generally more efficient [1, 30], and (2) electrode wear greatly increases due to the elevated discharge current. The electrical-to-thermal energy conversion efficiency also increases with increasing pressure, increased gap size, and reduced pulse energy [1, 30]. Due to the elevated electrode wear from SSB, PND igniters should be designed to avoid SSB.

While SSB-related electrode erosion issues can be mitigated through the use of dielectric electrode insulators that repel the discharge current [31, 32], the electric field strength becomes compromised with an associated decrease in radical formation rates. Instead it may be preferable to generate LTP without the use of dielectrics, with SSB instead inhibited through the selection of appropriate electrode geometry and pulse discharge characteristics. It is important to note that at engine-relevant pressures, LTP streamer propagation deviates from the well-established self-similar laws (i.e., increased streamer branching, thinner leader structures, and slower than expected streamer velocities) with unknown impact on discharge kinetics [33-35]. Potential causes for the scaling deviation at high-pressure include a change in electron recombination physics [33], less effective streamer cooling by thermal conductivity [36], and photoionization by excited-state nitrogen relaxation [34].

Direct imaging of single-pulse PND discharges using intensified cameras with short gate times (e.g. 5 ns) has provided insight into primary and secondary streamer propagation and structure [29, 37-39], specifically the impact of oxygen (O_2) and water concentration on streamer branching at atmospheric or sub-atmospheric pressure. Ono et al. [37] identified specific species produced during each streamer phase: the excited state transition of molecular nitrogen $N_2(C^3\Pi_u \rightarrow B^3\Pi_g)$ was observed in both the primary and secondary streamers, while atomic oxygen was inferred from ozone measurements to only be created in the secondary streamer. In this work, the $N_2(C^3\Pi_u \rightarrow B^3\Pi_g)$ transition was directly-imaged in order to visualize primary and secondary streamer structure, while O-atom was visualized using the $O(3p^3P \rightarrow 3s^3S)$ transition.

Previous engine research studies have investigated the use of multi-pulse PND operation, where close-coupled PND with pulse dwell times of ~100 µs were used to continuously augment radical production while ideally avoiding SSB [22, 23]. However, direct discharge imaging during stable engine operation revealed that SSB almost always occurred at some point during the pulse burst; an example image of the luminous SSB event from a 10-pulse burst from Sjöberg et al. [23] is shown in Figure 1. Moreover, once SSB occurred during the burst, each successive discharge in the pulse-burst exhibited SSB biased towards the same cathode site as the first SSB event. Wolk and Ekoto [40] identified fast-gas heating along streamer channels as a likely mechanism that leads to this behavior for PND in air. The impact of gas composition, specifically EGR constituents and fuel components, on SSB propensity in high-voltage PND has not yet been evaluated.

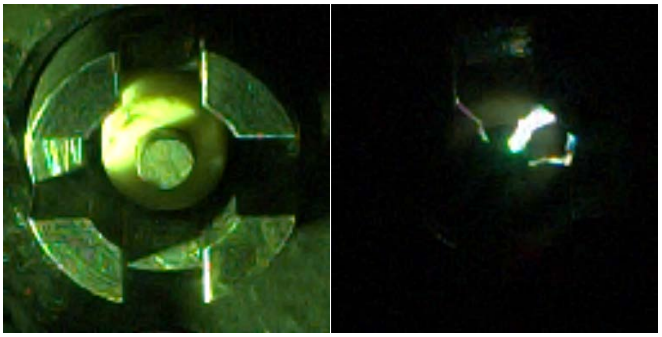

Figure 1. Image of a 4-prong PND plug in a single-cylinder research engine along with imaging for 10-pulse PND bursts with a 100 µs dwell between successive pulses. Intense luminosity between the central anode and one of four separated cathode sites is indicative of SSB.

The current paper describes experiments performed in a custom-built, optically accessible spark calorimeter used to evaluate high-voltage PND at engine-relevant densities, specifically in EGR-like gases at elevated pressure. For all experiments, the test gas mixture was a combination of ultra-air, N_2, carbon dioxide (CO_2), and water (H_2O) with a point-to-point electrode configuration selected so that the local E/N, and hence active radical formation, was maximized near the anode and cathode. Pressure-rise calorimetry was used to measure the electrical-to-thermal energy conversion efficiency for single-pulse PND discharges as a function of ambient pressure and gas composition. High-speed photodiode measurements were used to determine the SSB probability for each pressure and gas composition; the pulse electrical energy and electrical-to-thermal energy conversion efficiency were conditionally-averaged based on whether the PND remained an LTP or transitioned to a SSB discharge. Simultaneous direct imaging of excited-state O-atom and molecular nitrogen emission was performed for select LTP discharges at a range of initial pressures (P_{init}) and gas compositions to evaluate the impact on O-atom production and streamer structure.

Approach

All experiments were performed in a custom-built, optically accessible, spark calorimeter illustrated in Figure 2. The calorimeter body is constructed of 316 stainless steel, with a cylindrical 29 cm^3 internal chamber volume ($\mathcal{V}_{cal}$). An inlet port was used to fill the chamber to the desired pressure (up to 9 bar absolute) with a premixed ultra-air/N_2/CO_2/H_2O mixture. The gas mixture was prepared using MKS GE50A flow controllers and a syringe pump (Valcor SV690) and was stored in a 1-liter reservoir with a metered bypass valve. The calorimeter and reservoir were either unheated or heated to 70°C using resistive heating tape with the temperature monitored using embedded type-K thermocouples. The calorimeter thermocouple was installed flush with the wall of the calorimeter internal volume.

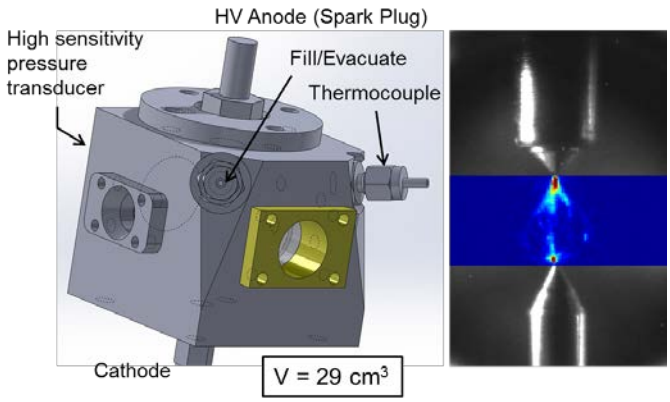

Figure 2. Illustration of the optically accessible spark calorimeter (left) and an image of the spark gap as visualized through the optical viewing port (right). An example image of filtered natural luminosity from the discharge has been superimposed between the electrodes.

The calorimeter body also features viewing access of the discharge event through an optical port on the front side wall along with input and output laser access ports that facilitate acquisition of laser-based spectroscopy measurements (not employed in this work). The 20 mm clear aperture viewing window enabled direct imaging of the discharge. The 16 mm diameter entrance and outlet laser windows had a 12.9 mm clear aperture and were installed orthogonal to the viewing window in opposing calorimeter sidewall ports. Calorimeter window ports included a 45° beveled seat and copper gasket that mated with a complementary bevel on the front window surface to provide a primary seal and minimize mechanical stresses that could induce window fracture when the calorimeter was pressurized. A metal retainer was used to secure the windows into the calorimeter via 4 screw holes that mated with tapped holes around the window ports; another copper gasket was placed between the retainer and the window back surface to minimize mechanical stresses. A Kalrez O-ring was placed into a machined O-ring grove in each window port to further prevent leakage around the windows when the calorimeter was pressurized.

To generate the PND within the spark calorimeter, a Transient Plasma Systems Inc. SSPG-101-HF high-voltage (28 kV peak) pulse generator with a 12 ns full width at half max (FWHM) pulse width and a 5 ns rise time was used. A low-impedance inline attenuator was used to monitor pulse voltage and current for each discharge event. The high-voltage anode was a modified NGK DP7EA-9 size M12 non-resistive sparkplug that was centrally positioned on the calorimeter top. The plug J-hook and the top 1 cm of material from the outer body ground was removed, with the anode tip machined to a rounded point (~125 µm radius of curvature) so that local electric field strengths were maximized, while maintaining relatively repeatable discharge characteristics. The cathode was replaced by a sharpened 3.18 mm diameter steel rod installed from the calorimeter base and secured in place by a Swagelok fitting. The inter-electrode distance between the anode and cathode was set to 5.0 mm. Alternatively, an "Anode-only" configuration was studied where the cathode was replaced by a stainless steel rod flush with the calorimeter interior bottom surface (19.6 mm from anode tip). Key calorimeter specifications and operating conditions are summarized in Table 1.

Table 1. Calorimeter specifications and operating conditions.

Calorimeter Internal Volume [cm^3]	29.0
Purge and fill cycle time [s]	105
Initial Temperature [°C]	70 ± 1.0, 21 ± 1.0
Initial Pressure [bar]	1.07 – 9.0
Gas Density [kg/m^3]	1.08 – 9.12
Inter-Electrode Distance [mm]	5.0, Anode Only
Electrode Tip Radius of Curv. [µm]	~125
Gas Mixtures [mole-%][†‡]	Ultra-air: 21.9% O_2, 78.1% N_2 (γ = 1.397) 15.9% O_2, 84.1% N_2 (γ = 1.397) 15.9% O_2, 78.8% N_2, 5.3% CO_2 (γ = 1.387) 15.9% O_2, 77.0% N_2, 3.7% CO_2, 3.4% H_2O (γ = 1.387)

[†]Ratio of specific heats (γ) calculated at 70 °C.
[‡]Additional minor species in ultra-air neglected.

Four gas compositions were studied: (1) ultra-zero air (Matheson) with 21.9 mole-% O_2, (2) ultra-zero air mixed with additional nitrogen to achieve 15.9 mole-% O_2, (3) ultra-zero air mixed with nitrogen and CO_2 to achieve 15.9 mole-% O_2 and 5.3 mole-% CO_2, and (4) ultra-zero air mixed with nitrogen, CO_2, and H_2O to achieve 15.9 mole-% O_2, 3.7 mole-% CO_2, and 3.4 mole-% H_2O. The concentrations of O_2 and CO_2 in the tested gas mixtures were verified using a CAI 600 Series multi-gas analyzer. The O_2 concentration of 15.9% was adopted from the intake composition estimated from experimental engine data from Argonne National Laboratory using a similar PND system [22]: 15.9% O_2, 3.7% CO_2, 3.4% H_2O, 77.0% N_2 (excluding hydrocarbons). In [22], the 12.1:1 compression ratio engine was operated at 1500 rpm, 5.6 bar indicated mean effective pressure (IMEP), and 23 mole-% EGR. The CO_2 concentration of 5.3% in the ultra-air/N_2/CO_2 mixture was chosen to achieve the same heat capacity as the intake composition in [22] in order to isolate the impact of H_2O from changes in heat capacity. Although not included in this work, the presence of hydrocarbons may have an important impact on discharge behavior and will be evaluated in a future study.

Pressure-Rise Calorimetry

For the calorimetry experiments, P_{init} was varied between 1.07 bar and 9 bar absolute with initial temperatures fixed at 70 ± 1.0 °C. For these conditions, the chamber gas densities were similar to the densities encountered in the engine in [22]. This is illustrated in the upper plot of Figure 3 where the in-cylinder density from the fired engine in [22] is plotted versus crank angle, with the densities tested in the calorimeter indicated for the range of P_{init}. The spark timing from the engine experiments is indicated in Figure 3 by the vertical dashed line – the in-cylinder density at the time of spark was equivalent to P_{init} = 4.75 bar in the calorimeter. The in-cylinder pressure and bulk-averaged temperature from [22] are also plotted versus crank angle in the bottom of Figure 3 for reference.

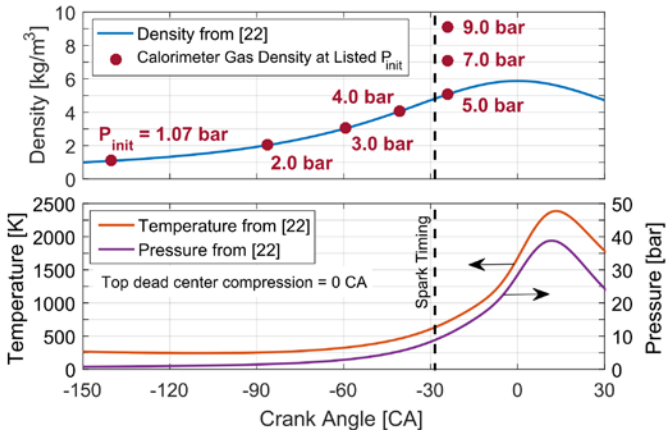

Figure 3. In-cylinder density (top), temperature (bottom), and pressure (bottom) as a function of crank angle for a fired engine experiment in [22]. The densities tested in the calorimeter are indicated for the range of P_{init}.

The calorimeter gas densities for P_{init} = 7.0 bar and P_{init} = 9.0 bar were greater than the top dead center density from the engine experiments. However, note that the intake was slightly throttled in [22] such that the intake pressure was ~71 kPa (absolute). If the engine in [22] was operated at an intake pressure of ~105 kPa, the gas density at the time of spark would be equivalent to the calorimeter gas density for P_{init} = 7.0 bar. Similarly, the calorimeter gas density at P_{init} = 9.0 bar would be representative of the engine operated at an intake pressure of ~135 kPa.

For each gas composition, initial pressure, and electrode configuration studied, 30 calorimetry runs were performed. To ensure that residual discharge products did not persist between runs and possibly influence the subsequent discharge, chamber contents after each run were cycle-purged twice using fill and vacuum solenoid valves connected to the gas supply and an available vacuum turbo-pump, respectively. Chamber fill pressure was accurately controlled using a Proportion-Air QPV pressure control valve. Differential chamber pressures were measured using a PCB 106B51 high-sensitivity pressure transducer (145 µV/Pa). The transducer was secured to the calorimeter using an acetal mounting adapter for electrical isolation with the signal amplified by a Kistler 5134B coupler. All data were recorded using a LeCroy HDO 6054 500 MHz high-definition oscilloscope. Recorded pressures were filtered by a 1 kHz low-pass filter during post-processing to remove noise from the discharge event. The SSB probability at each condition was determined from light emission recorded by a Thorlabs DET210 high-speed photodiode placed against an available window port.

Electrical-to-thermal energy conversion efficiency — defined here as the thermal energy deposited into the gas (E_{therm}) normalized by the pulse electrical energy delivered (E_{elec}) to the igniter — was determined for each discharge. Pulse electrical energy was obtained by direct integration of the instantaneous electrical power (W), calculated from the product of the inline attenuator voltage (V) and current (I) measurements over the length of each pulse (t_p):

$$E_{elec} = \int_0^{t_p} W(t)dt = \int_0^{t_p} V(t)I(t)dt \qquad (1)$$

Gas thermal energy deposition was determined from the volumetric integration of the change in internal energy (δu):

$$E_{therm} = \int \delta u d\mathcal{V} = \int \rho c_v \Delta T d\mathcal{V} = \left(\frac{c_v}{R}\right)\mathcal{V}_{cal}\Delta P = \frac{\mathcal{V}_{cal}\Delta P}{\gamma - 1} \qquad (2)$$

where ρ, R, c_v, and γ respectively are the density, gas constant, volumetric heat capacity, and specific heat ratio of the gas mixture. The pressure-rise (ΔP) was the highest recorded differential pressure measurement from a calorimetry experiment. Due to the small pressure-rises encountered in the experiments, a constant γ based on the gas composition and initial temperature was assumed.

Direct Imaging of Discharge

For the direct imaging experiments, P_{init} was varied between 1.7 bar and 2.0 bar absolute with initial temperatures fixed at 21 ± 1.0 °C. A lower temperature was used for the imaging studies compared to the calorimetry because no image signal was observed for LTP-only conditions at 70°C. The limited pressure range studied at 21°C was a result of SSB occurrence preventing imaging below P_{init} = 1.7 bar and an absence of signal for P_{init} > 2.0 bar.

In order to qualitatively evaluate the production and distribution of atomic oxygen, direct imaging was performed using the O($3p^3P \rightarrow 3s^3S$) transition at 844.9 nm. Excitation of atomic oxygen to the O($3p^3P$) state occurred via electron impact excitation during the discharge and emission at 844.9 nm was isolated using a narrowband interference filter centered at 840 nm with 10 nm bandwidth (Andover 840FS10-50; 57% transmission at 844.9 nm). Light emitted from the discharge through the viewing window was separated using a dichoric beam splitter at 45° angle of incidence with high transmissivity (>98%) at 844.9 nm and high reflectivity (>95%) from 310 nm to 360 nm (Lattice Electro Optics LWP-45-R337.1-T844.9-UF-2025), as shown in Figure 4. To determine the streamer structure, direct imaging of excited state N_2 transitions near the $N_2(C^3\Pi_u \rightarrow B^3\Pi_g)$ transition at 337.1 nm was performed simultaneously with the O($3p^3P \rightarrow 3s^3S$) imaging by using the unfiltered reflection from the dichoric beam splitter.

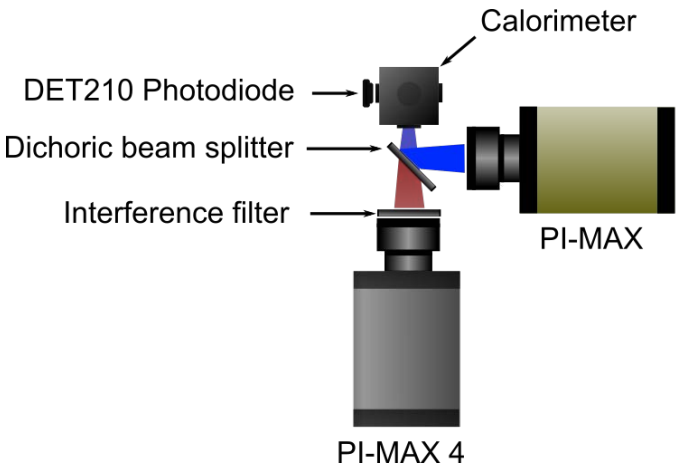

Figure 4. Diagram of the imaging setup used to simultaneously image excited state transitions of O-atom (PI-MAX 4; 844.9 nm) and N_2 (PI-MAX; transitions near 337.1 nm).

O-atom emission images were recorded using a Princeton Instruments PI-MAX 4: 1024 EM intensified camera with a 1024×1024 pixel imaging array, 2x2 hardware binning, an 85 mm *f*/1.8 Nikkor lens, and a 56 mm extension tube. The PI-MAX 4 was operated at a gain (G) setting between G = 400 and G = 10,000 (maximum) with gate durations of 5 ns or 500 ns. The gate duration of 5 ns was used to capture time-resolved excited-state O-atom images, while the 500 ns gate duration was used to image the entire discharge event. Similarly, N_2 emission images were recorded using a

Princeton Instruments PI-MAX intensified camera with a 512×512 pixel imaging array, an 85 mm *f*/1.8 Nikkor lens, and a 56 mm extension tube. The PI-MAX was operated at maximum gain (G = 255) with 500 ns gate duration only. To prevent intensifier damage for both cameras, only consistent LTP conditions (i.e. SSB probability equals zero) were imaged.

In order to increase the data acquisition rate for the direct imaging experiments, the pressure transducer was removed and replaced with a metal plug containing a threaded outlet port. The desired gas mixture flowed continuously through the calorimeter with discharges at 10-second intervals (>2 calorimeter flow through times), for a total of 30 discharges using the 500 ns gate duration. For the 500 ns gate duration imaging, the intensifier gate delays were adjusted to achieve coincidence of the intensifier gate timing between the two cameras, verified using a high-speed oscilloscope. For the 5 ns gate duration, 100 discharges were recorded at each tested operating condition. Only one image could be recorded per discharge; however, normally-distributed jitter in the start of discharge time (σ = 60 ns) led the 5 ns gate duration images to span a range of times after the discharge. The image time relative to the start of the discharge was determined in post-processing using the intensifier monitor signal from the PI-MAX 4 and the rising edge of the discharge voltage trace.

Images from each camera were separately background subtracted and flat-field corrected. The intensity of excited-state O-atom images collected using G < 10,000 were corrected up to G = 10,000 on a pixel-by-pixel basis using the ratio of the flat-field images at the G used (e.g. G = 400) and G = 10,000. As a result, unless otherwise noted, the intensity of all images for each gate duration can be directly compared. Average images for the 500 ns gate duration were constructed by median-averaging the image sets on a pixel-by-pixel basis. The 5 ns gate duration images were spatially median-filtered using a 5×5 pixel window.

Results and Discussion

Pressure-Rise Calorimetry

SSB Propensity

Fundamental knowledge of the SSB propensity of PND in air and EGR-like gas mixtures will facilitate the development of strategies to avoid SSB in automotive engines. To this end, the SSB occurrence probability was determined for the gas mixtures listed in Table 1 as a function of P_{init} from 1.07 bar to 9.0 bar at 70°C using the 5.0 mm gap, with the results plotted in Figure 5. The Anode-only configuration was also evaluated for the 21.9% O_2 mixture. The filled symbols in Figure 5 indicate experiments that were conducted using a different bottle of ultra-air than the open symbols – the impact of the change in ultra-air bottle will be discussed later in this section.

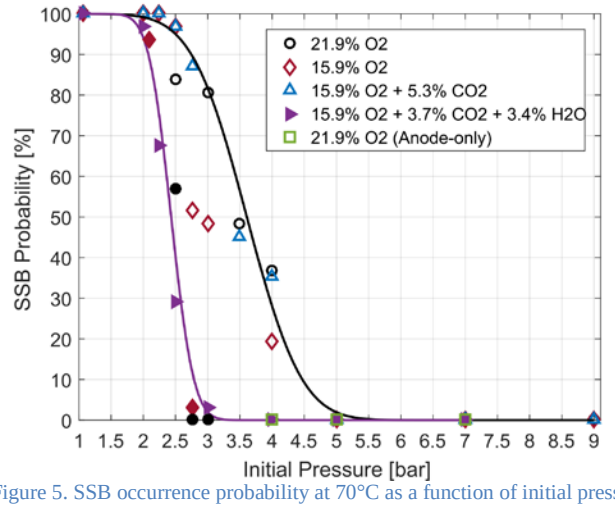

Figure 5. SSB occurrence probability at 70°C as a function of initial pressure and gas composition for a single ~24 kV_{peak} discharge using the 5.0 mm gap. 30 experiments were conducted at each condition. The solid lines are inverse error function curve fits. Filled symbols indicate data points that were taken using a different ultra-air bottle compared to the open symbols.

Looking first at the open symbols in Figure 5, the SSB occurrence probability did not depend appreciably on the O_2 or CO_2 mole fractions at the tested conditions. For all tested gas mixtures, the discharge exhibited 100% SSB occurrence at $P_{init} \leq 2.0$ bar. For P_{init} > 2.0 bar, the SSB occurrence probabilities decreased with increasing pressure. For the 5 mm gap at $P_{init} \geq 5.0$ bar, only LTP discharges were observed.

The Anode-only configuration was run for $P_{init} \geq 4.0$ bar as arcing upward towards the calorimeter top was observed for P_{init} < 4.0 bar, potentially along the ceramic insulator of the spark plug. The Anode-only configuration operated as a LTP discharge at P_{init} = 4.0 bar, where the SSB occurrence probability was near 30% for the 5 mm gap. This illustrates the main advantage of the Anode-only configuration: to reduce the occurrence of SSB.

The SSB occurrence probability curve shifted to lower pressures with the change in ultra-air bottle (filled symbols in Figure 5), so repeat conditions for the 21.9% O_2 and 15.9% O_2 mixtures were run to compare to the 15.9% O_2 + 3.7% CO_2 + 3.4% H_2O gas mixture. From the filled symbols in Figure 5, it is evident that the SSB occurrence probability did not depend appreciably on the H_2O or CO_2 concentrations examined. However, it can be inferred that some change in the ultra-air composition decreased the SSB occurrence probability for pressures between 2 bar and 5 bar. The authors speculate that the argon concentration may have decreased between the first and second ultra-air bottles, although argon concentration information was not available for the ultra-air used in this study.

Pulse Electrical Energy

The decreasing SSB propensity with increasing P_{init} indicates that the nature of the discharge was changing. The change in the nature of the discharge with P_{init} was also evident in the pulse electrical energy, calculated by integration of the product of the measured voltage and current. The pulse electrical energy is presented in Figure 6 for the four tested gas mixtures as a function of P_{init} at 70°C for the 5 mm gap and Anode-only configuration. The pulse electrical energy was conditionally-averaged based on whether the PND remained an LTP or transitioned to a SSB discharge. The conditionally-averaged LTP

and SSB pulse electrical energies were unaffected by the change in the ultra-air composition, despite the fact that the SSB probability changed. This can be seen by the similar values for the open and filled symbols for the 21.9% O_2 and 15.9% O_2 gas mixtures in Figure 6. Note that the scatter was larger for the LTP discharges at the lower P_{init} because the statistics were based on a small number of LTP discharges from the 30 calorimetry runs.

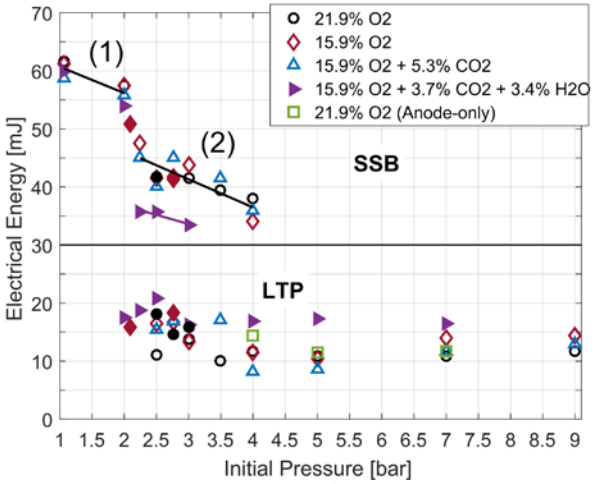

Figure 6. Average pulse electrical energy for SSB discharges (above horizontal black line) and LTP discharges (below horizontal black line) as a function of initial pressure and gas composition at 70°C. Two SSB regimes are evident, denoted by (1) and (2). Data are shown for a 5.0 mm gap and an Anode-only configuration. Filled symbols indicate data points that were taken using a different ultra-air bottle compared to the open symbols.

Similar to the SSB occurrence probability, the pulse electrical energy in Figure 6 did not depend appreciably on the O_2 or CO_2 mole fractions. Across the sweep of P_{init}, the LTP discharges for the 5.0 mm gap had pulse energies consistently near 14 mJ. The Anode-only configuration was only used at $P_{init} \geq 4.0$ bar and exhibited similar pulse electrical energy to the 5.0 mm gap. On the other hand, the SSB discharge had pulse energies of ~60 mJ at P_{init} = 1.07 bar with decreasing pulse electrical energy for increased P_{init}. The character of the SSB discharges changed for P_{init} > 2.0 bar, with a corresponding step-reduction in the pulse electrical energy. The two SSB regimes are denoted by (1) and (2) in Figure 6, and will be referred to as SSB Type 1 and SSB Type 2 throughout this paper.

The pulse electrical energy in Figure 6 for the 15.9% O_2 + 3.7% CO_2 + 3.4% H_2O gas mixture was similar to the other gas mixtures for the SSB Type 1 and LTP discharges, but lower for the SSB Type 2 discharges (between P_{init} = 2.25 and 3.0 bar). The reason for the disparity for the SSB Type 2 discharges will be discussed in the next paragraph.

To illustrate the differences between SSB Type 1, SSB Type 2, and LTP discharges, selected discharge traces of voltage, current, and integrated power are presented in Figure 7 for 15.9% O_2 at (a) P_{init} = 1.07, (b) P_{init} = 3.0, and (c) P_{init} = 5.0 bar at 70°C for the 5.0 mm gap. For the SSB Type 1 discharge in Figure 7a, the breakdown occurred rapidly after the initial voltage rise. The corresponding increase in current flow limits the peak voltage reached to ~18 kV. The integrated power (i.e., pulse energy) increased relatively smoothly during the SSB Type 1 discharge to its final value near ~60 mJ. Differently, the LTP discharge shown in Figure 7c had high current flow only during the initial voltage rise and the peak voltage reached was near 24 kV. As only a fraction of the pulse energy was deposited into the LTP discharge, the majority the pulse was reflected back from the anode, as seen by the trough at ~100 ns in the integrated power trace after the initial hump. As the pulse continued to reflect back and forth between the anode and the pulse generator, it was damped from the cable resistance. This led to damped, oscillating voltage and current profiles, with the integrated power settling to a final value near 10 mJ (almost the same value as after the first reflection).

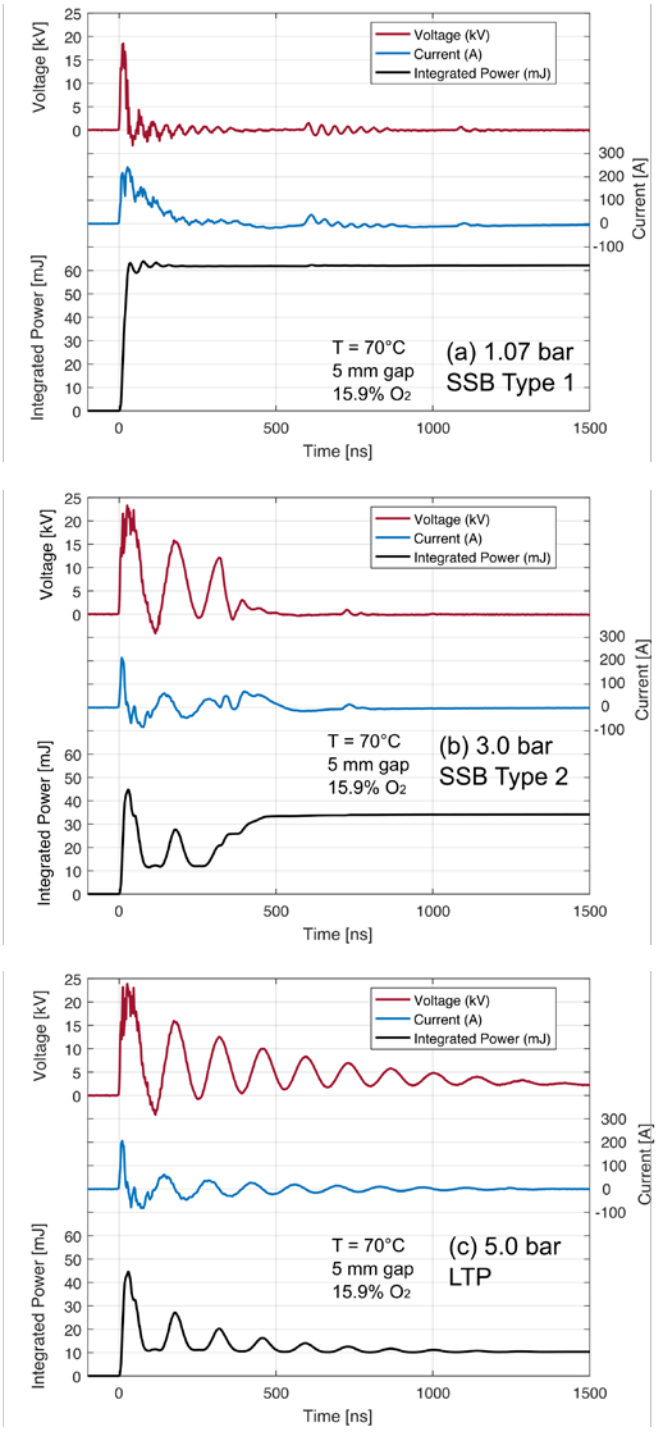

Figure 7. Instantaneous voltage, current, and integrated power in 15.9% O_2 at T = 70°C from: (a) SSB Type 1 discharge at 1.07 bar, (b) SSB Type 2 discharge at 3.0 bar, and (c) LTP discharge at 5.0 bar.

In between the SSB Type 1 and LTP discharges, the SSB Type 2 discharge shown in Figure 7b behaved as an LTP discharge for the first ~300 ns after the start of voltage rise. After this point, breakdown occurred, and the energy remaining in the damped, reflected pulse was deposited into the discharge. As a result, the pulse energy was ~33 mJ, in between the SSB Type 1 and LTP discharges. To the best knowledge of the authors, the classification of SSB Type 2 discharges has not been previously discussed in the literature.

The breakdown for SSB Type 2 discharges in the 15.9% O_2 + 3.7% CO_2 + 3.4% H_2O gas mixture occurred later in the reflected pulse compared the other tested gas mixtures, which caused the SSB Type 2 pulse electrical energy to be lower for the H_2O-containing mixture. For example, at P_{init} = 2.5 bar, the SSB occurrence was delayed by approximately one pulse reflection (~100 ns) for the H_2O-containing mixture compared to the 21.9% O_2 mixture. The three discharge types illustrated in Figure 7 led to different behavior with respect to the electrical-to-thermal energy conversion efficiency.

Electrical-to-Thermal Energy Conversion Efficiency

The electrical-to-thermal energy conversion efficiency is presented in Figure 8 for the four tested gas mixtures as a function of P_{init} at 70°C for the 5 mm gap and Anode-only configuration. The electrical-to-thermal energy conversion efficiency was conditionally-averaged based on whether the PND remained an LTP or transitioned to a SSB discharge. Similar to the pulse electrical energy, the conditionally-averaged LTP and SSB pulse electrical-to-thermal energy conversion efficiencies were unaffected by the change in the ultra-air composition. This can be seen by the similar values for the open and filled symbols for the 21.9% O_2 and 15.9% O_2 gas mixtures in Figure 8.

At P_{init} = 1.07 bar in Figure 8, the SSB (Type 1) electrical-to-thermal energy conversion efficiency was ~60%. As P_{init} was increased to 2.0 bar, the electrical-to-thermal energy conversion efficiency for the SSB (Type 1) discharge increased to ~85%. The transition of the SSB discharge to Type 2 occurred for P_{init} > 2 bar, with the energy conversion efficiency increasing further to ~90% at P_{init} = 2.25 bar. At P_{init} = 2.25 bar, the breakdown event was still closely-coupled to the initial voltage rise; thus, the discharge was relatively efficient with added efficiency benefits from the increased pressure and the decreased pulse energy compared to the SSB Type 1 discharge at P_{init} = 2.0 bar. As P_{init} increased further to 2.75 bar, the electrical-to-thermal energy conversion efficiency of the SSB Type 2 discharge fell because the breakdown event became more removed from the initial voltage rise. As P_{init} increased above 2.75 bar, the energy conversion efficiency increased, albeit at a slower rate than the SSB Type 1 discharge. The high pulse energy, high electrical-to-thermal conversion efficiency, and narrow arc structure of SSB discharges imply that high gas temperatures were achieved in these discharges and that ignition by such discharges would be a primarily thermal process.

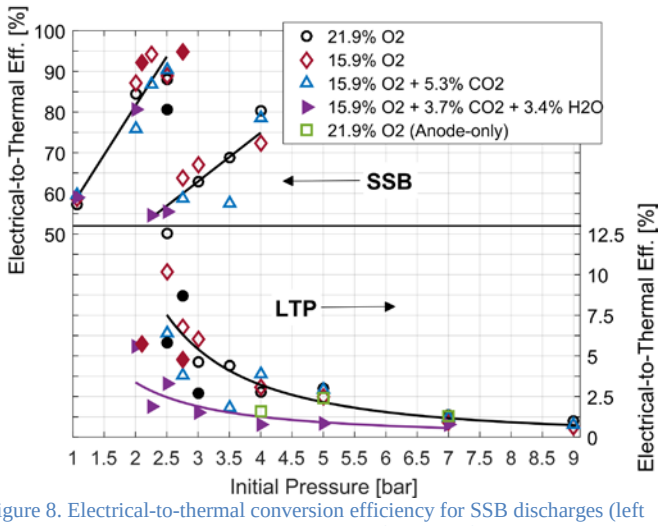

Figure 8. Electrical-to-thermal conversion efficiency for SSB discharges (left y-axis) and LTP discharges (right y-axis) as a function of initial pressure and gas composition at 70°C. The H_2O-containing mixture exhibits lower LTP discharge electrical-to-thermal conversion efficiencies than the other tested gas mixtures, despite good agreement with those gas mixtures for SSB discharges. Filled symbols indicate data points that were taken using a different ultra-air bottle compared to the open symbols.

In Figure 8, the first LTP discharges appear at P_{init} = 2.0 bar with conversion efficiencies near ~10%. Note that the scatter was larger at the lower P_{init} because the statistics were based on a small number of LTP discharges from the 30 calorimetry runs. As P_{init} increased, the LTP discharges exhibited monotonically-decreasing energy conversion efficiency. At P_{init} = 5.0 bar, the conversion efficiency was ~2.5%, decreasing to ~1% at P_{init} = 9.0 bar. The Anode-only configuration had LTP discharge energy conversion efficiencies similar to the 5.0 mm gap.

The 15.9% O_2 + 3.7% CO_2 + 3.4% H_2O mixture exhibited similar electrical-to-thermal energy conversion efficiencies compared to the other tested gas mixtures for SSB discharges. However, the LTP energy conversion efficiency was lower for the H_2O-containing mixture compared to the other tested gas mixtures for P_{init} < 7 bar. The mechanism by which H_2O reduced the percentage of electrical energy that was converted to thermal energy for the LTP discharges has not yet been identified. However, it was observed that the discharge current rise was delayed by about 2 ns for the H_2O-containing mixture compared to the 21.9% O_2 mixture, which may indicate that H_2O fundamentally impacted the streamer discharge process.

Summary of calorimetry results

From an SSB occurrence probability, pulse energy, and electrical-to-thermal energy conversion efficiency perspective, variations in O_2 and CO_2 mole fractions typical of engine operation (0-23% EGR) did not have a major impact on PND behavior. However, the addition of H_2O to the gas mixture had two measureable effects: (1) reduction of the pulse electrical energy for SSB Type 2 discharges by delaying the breakdown event further from the start of voltage rise, and (2) reduction of the electrical-to-thermal energy conversion efficiency for LTP discharges at P_{init} < 7 bar. Additionally, the performance of the Anode-only configuration was similar to the 5 mm gap, except that the SSB occurrence probability was reduced from ~30% to zero at P_{init} = 4.0 bar.

Direct Imaging of Discharge

Time-resolved imaging

Increasing P_{init} resulted in a clear reduction in the electrical-to-thermal energy conversion efficiency for LTP discharges. However, the calorimetry results do not provide insight into changes in O-atom production with increasing P_{init}, an important factor for LTP ignition in automotive engines [8]. Therefore, the impact of increasing P_{init} on O-atom production was evaluated using direct imaging.

Single-shot images (5 ns gate duration) of the electronically-excited O-atom transition 8 ns – 62 ns after the start of voltage rise are presented in Figure 9 (on Page 11) for 21.9% O_2 at 1.7 bar and 2.0 bar. These images were taken when the gas temperature was 21°C (calorimeter unheated) and at a lower peak voltage setting (18 kV_{peak} compared to 24 kV_{peak}) than the calorimetry data because no signal was obtained at LTP-only conditions for the 70°C cases ($P_{init} \geq 5$ bar). All images in Figure 9 have been corrected such that their intensities can be directly compared. Sample voltage and current traces for P_{init} = 1.7 bar are shown in Figure 10 for reference (the voltage and current profiles are very similar for P_{init} = 2.0 bar).

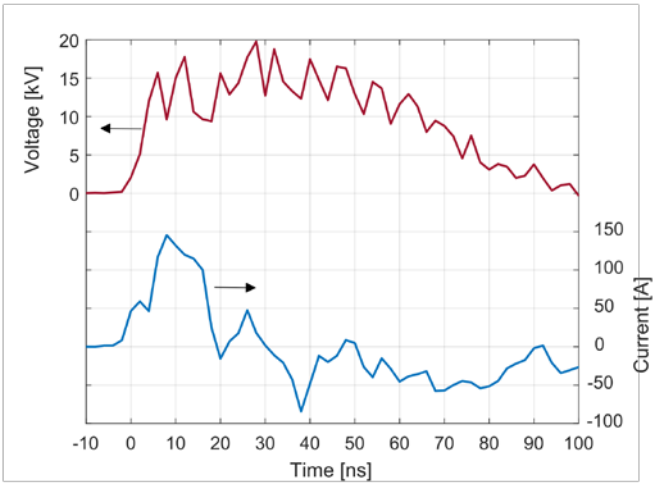

Figure 10. Sample voltage and current profiles for the first 100 ns after the start of voltage rise at P_{init} = 1.7 bar and 21°C (used as a reference for images in Figure 8).

Looking first at the P_{init} = 1.7 bar images (top row) in Figure 9, strong signal was observed at the anode and cathode 8 ns after the start of voltage rise, which corresponds to the peak discharge current (see Figure 10). Signal was observed about 1 mm below the anode and 2 mm above the cathode, with minimal signal from 1-2 mm below the anode. These images indicate that the concentration of electric field lines at the anode and cathode tips resulted in regions of strong electronically-excited O-atom production. These results imply that the presence of the cathode was beneficial for increasing radical production during the discharge compared to an Anode-only configuration. The improvement in radical production provided by the cathode further suggests that electrode designs for use in automotive engines should incorporate a cathode, as long as SSB can be avoided.

The condition imaged in Figure 8 resulted only in LTP discharges, which means that the secondary streamer did not propagate across the gap to the cathode (if it did, SSB would have occurred). Therefore, the presence of electronically-excited O-atom signal near the cathode tip indicates that the primary streamer resulted in substantial O-atom production and electronic excitation. This observation is contrary to the theory proposed by Ono et al. [37] where it was inferred from ozone (O_3) measurements that O-atom was produced primarily by the secondary streamer. While O_3 is mainly created from the reaction $O + O_2 + M \rightarrow O_3 + M$, O-atom is primarily produced by electron-impact dissociation of O_2 from high energy electrons (i.e., $e + O_2$) [37]. While Ono et al. [37] was correct to infer that O-atom was present during the secondary streamer to participate in the O_3 formation reaction, the majority of O-atom was likely created in the primary streamer. For the discharge in Figure 8, the higher electric fields in the primary streamer resulted in more efficient electron-impact dissociation of O_2 compared to the secondary streamer, despite the shorter residence time of the primary streamer compared to the secondary streamer (primary streamer lifetime was O(1 ns) compared to O(10 ns) for the secondary streamer).

Similar observations to those at 8 ns can be made at 20 ns after the start of voltage rise, where the current was near zero, but the electronically-excited O-atom signal remained strong. By 30 ns, the signal weakened in the middle of the gap, but remained high near the anode and cathode. The signal continued to weaken with increasing time, and no signal was observed at or after 62 ns. Note that this does not mean that there was no ground state O-atom at this point, only that the $O(3p^3P \rightarrow 3s^3S)$ transition was not sufficiently active to be observed. Previous O-atom two-photon laser induced fluorescence measurements performed by the authors at P_{init} = 1.7 bar measured ground state O-atom at up to 200 µs after the discharge [40]. Therefore, ground state O-atom likely existed at 62 ns, but there were not sufficient high-energy free electrons to excite ground state O-atom to the $O(3p^3P)$ state (11 eV).

Similar behavior to that observed at P_{init} = 1.7 bar was observed at P_{init} = 2.0 bar, as seen in the bottom row of Figure 9. The main differences at P_{init} = 2.0 bar compared to P_{init} = 1.7 bar are: (1) thinner structures, (2) decreased signal levels, and (3) more rapid disappearance of the signal with increasing time. Neglecting changes in species produced by the discharge, the collisional de-excitation (quenching) of the $O(3p^3P)$ state increased as the ratio of the pressures (~20%). However, the differences in signal due to quenching alone do not account for the variation in signal between the two pressures. Therefore, it is assumed that the decreased E/N resulted in lower energy free electrons, reduced production of O-atom, and decreased excitation of O-atom to the $O(3p^3P)$ state. The effects of quenching and electron energy will be evaluated in detail in a later section. At pressures above P_{init} = 2.0 bar, no signal was observed for these conditions.

Entire discharge imaging

Although changes in the O_2 and CO_2 mole fractions did not have an appreciable impact on the calorimetry results, measurable impact on O-atom production/excitation and N_2 excitation was observed (the mixture containing H_2O could not be studied in the unheated calorimeter). Median images of the entire discharge (500 ns gate duration) are presented in Figure 11 (on Page 11) for the non-H_2O containing gas mixtures at P_{init} = 1.7 bar and/or P_{init} = 2.0 bar. Images of the excited state O-atom transition are shown in the top row of Figure 11, while images of the excited state N_2 transitions are presented in the bottom row. The images in each row have been corrected such that their intensities can be directly compared, except that the intensity of the 15.9% O_2 + 5.3% CO_2 images have been multiplied by 2 for clarity.

Focusing first on the 21.9% O_2 condition at P_{init} = 1.7 bar in Figure 11, strong electronically-excited O-atom signal was observed near the anode and cathode with weaker signal near the center of the gap. The electronically-excited N_2 image shows similar characteristics to the electronically-excited O-atom image, but the regions of high signal intensity near the anode and cathode are thinner and extend further into the gap. When the initial pressure was increased to P_{init} = 2.0 bar at 21.9% O_2, the signal intensity of both the electronically-excited O-atom and N_2 images decreased, similar to the behavior observed in Figure 9.

Reducing the O_2 concentration to 15.9% at P_{init} = 2.0 bar led to increased electronically-excited N_2 signal and reduced electronically-excited O-atom signal compared to 21.9% O_2, but the major features of the discharge remained unchanged. The 15.9% O_2 mixture could not be run at 1.7 bar due to non-zero SSB occurrence probability.

The addition of 5.3% CO_2 to the 15.9% O_2 mixture greatly reduced the signal observed in both the electronically-excited O-atom and N_2 images at P_{init} = 1.7 bar, as seen in Figure 11. No signal was observed for the 15.9% O_2 + 5.3% CO_2 mixture at P_{init} = 2.0 bar.

The changes in the observed image intensities were confounded by changes in collisional quenching, the effect of which will be evaluated in the next section.

The impact of collisional quenching on image intensity

The impact of collisional quenching of the targeted excited states at the P_{init} and gas compositions used for the imaging studies can be evaluated by comparing the fluorescence quantum yields (a), as described by Equation 3 [41]. The fluorescence quantum yield is the ratio of the rate of spontaneous emission (A) divided by the sum of A and the collisional quenching rate (Q). In other words, a is the fraction of an excited state species that relaxes via photon emission compared to collisional de-excitation. The collisional quenching rate was computed using Equation 4 [41], where k_i is the quenching rate coefficient of species i and n_i is the number density of species i.

$$a = \frac{A}{A+Q} \quad (3)$$

$$Q = \sum_i k_i n_i \quad (4)$$

The spontaneous emission rate and quenching rate coefficients are presented in Table 2 for the excited states $O(3p^3P)$ and $N_2(C^3\Pi_u)$, where $N_2(C^3\Pi_u)$ has been chosen to represent the imaged N_2 transitions.

Table 2. Spontaneous emission (A) and quenching rate (k_i) coefficients.

	$O(3p^3P \rightarrow 3s^3S)$	$N_2(C^3\Pi_u \rightarrow B^3\Pi_g)$
A [10^7 s^{-1}]	2.88 [41]	2.38 [42]
k_{O2} [10^{-16} m^3s^{-1}]	9.4 [41]	3.0 [42]
k_{N2} [10^{-16} m^3s^{-1}]	5.9 [43]	0.11 [42]
k_{CO2} [10^{-16} m^3s^{-1}]	6.6 [44]	3.9 [42, 45]

The quenching rate was estimated using n_i calculated at P_{init} and 21°C with the species mole fractions from Table 1. The estimated fluorescence quantum yields are presented in Table 3 for the three tested gas mixtures at P_{init} = 1.7 and 2.0 bar. Note that a was nearly constant across the tested gas mixtures for the $O(3p^3P \rightarrow 3s^3S)$ transition.

Table 3. Estimated fluorescence quantum yields (a) at P_{init} = 1.7 and 2.0 bar.

	$O(3p^3P \rightarrow 3s^3S)$		$N_2(C^3\Pi_u \rightarrow B^3\Pi_g)$	
Gas Mixture	a(1.7 bar) [%]	a(2.0 bar) [%]	a(1.7 bar) [%]	a(2.0 bar) [%]
21.9% O_2	0.101	0.086	0.747	0.636
15.9% O_2	0.104†	0.089	0.972†	0.828
15.9% O_2 + 5.3% CO_2	0.104	0.088†	0.721	0.613†

†Condition not used for imaging studies.

Increasing P_{init} from 1.7 to 2.0 bar at 21.9% O_2 decreased a by ~20% for both the $O(3p^3P)$ and $N_2(C^3\Pi_u)$ states. The observed decreases in image intensity seen in Figure 11 were greater than the decrease in a, which implies other factors were at play, such as changes in the electron energy distribution.

Decreasing the O_2 concentration to 15.9% from 21.9% at P_{init} = 2.0 bar led a for the $O(3p^3P)$ state to increase slightly, yet a decrease in image intensity was observed in Figure 11. The reduction in electronically-excited O-atom image intensity may be due to the ~30% reduction in the mole fraction of O_2 present in the gas mixture (15.9% versus 21.9%). For the $N_2(C^3\Pi_u)$ state, a increased by ~30% which is consistent with the change in image intensity observed in Figure 11. The increase in a was more than the increase in the mole fraction of N_2 in the gas mixture (~8%).

Changing the gas mixture from 21.9% O_2 to 15.9% O_2 + 5.3% CO_2 at P_{init} = 1.7 bar led a for the $O(3p^3P)$ state to increase slightly and a for the $N_2(C^3\Pi_u)$ state to decrease by ~4%. The observed decrease in image intensity is much larger than the change in a, which suggests another mechanism was dominant for suppressing creation of and/or emission from the targeted excited states.

The impact of the electron energy distribution on image intensity

Another main factor that could have influenced the observed signal was the energy distribution of the electron population because excitation of O-atom and N_2 to the targeted excited states was accomplished though electron impact excitation from high-energy free electrons present in the discharge. The energy distribution of the electron population can be described by the electron energy distribution function (EEDF). Estimation of the EEDF for the tested gas mixtures at each P_{init} was used to provide insight into how changes in gas composition and P_{init} affected the electron energy distribution, and thus the observed signal.

The EEDF was estimated through multiple steps. First, the electric field was estimated using the MATLAB PDE Toolbox [46] with a 3D model of the calorimeter internal surfaces. The anode surface was set to the measured peak voltage with all other surfaces set to ground. The electric field strength just below the anode was extracted to calculate the reduced electric field (E/N), where N was computed using the initial number density. The estimated E/N were 460 Td at P_{init} = 1.7 bar and 390 Td at P_{init} = 2.0 bar. Finally, the mole fractions

of O_2, N_2, and CO_2 from Table 1 were used to evaluate the EEDF at the estimated E/N in BOLSIG+ [47] only considering collisions with O_2, N_2, and CO_2.

The computed EEDF for the three tested gas mixtures at P_{init} = 1.7 and 2.0 bar are presented in Figure 12. Increasing P_{init} resulted in noticeable changes to the EEDF, namely decreasing the average electron energy, which is consistent with the decreasing signal observed for the 21.9% O_2 condition with increasing P_{init}. On the other hand, changes in gas composition had only minor impact on the EEDF. Furthermore, the 15.9% O_2 + 5.3% CO_2 mixture had similar average electron energy to the other tested gas mixtures, but the weakest signal in Figure 11. Therefore, changes in the observed signal in Figure 11 for the 15.9% O_2 + 5.3% CO_2 mixture were not attributable to changes in collisional quenching or the EEDF. These results imply that the presence of 5.3% CO_2 in the gas mixture reduced the production and excitation of O-atom through another route, potentially by increasing the rate of O-atom reaction to O_2 [48]. Deeper analysis of how the EEDF impacted the creation and/or excitation of O-atom and N_2 requires more detailed kinetic modeling that is outside the scope of this paper.

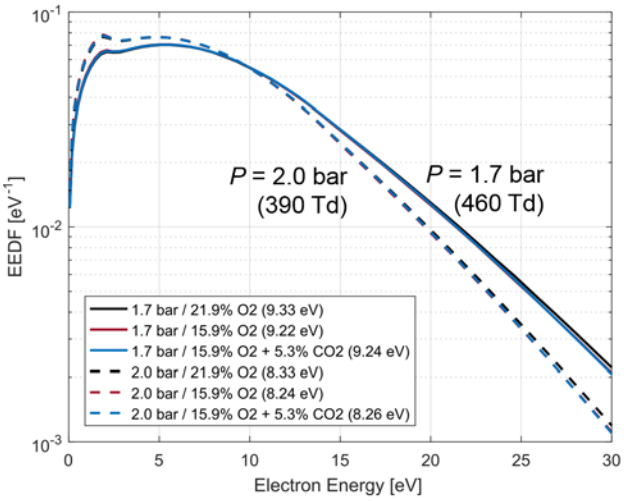

Figure 12. Computed EEDFs in BOLSIG+ considering collisions with O_2, N_2, and CO_2 for LTP discharges at P_{init} = 1.7 and 2.0 bar at 21°C. Average electron energies are indicated in the legend.

Summary of direct imaging results

The primary streamer was found to generate substantial excited-state O-atom, specifically near the anode and cathode tips where electrical field strengths were highest. These results suggest that the presence of a cathode is desirable for electrodes used in automotive engines. Increased P_{init} led to weaker excited state O-atom signal, thinner structures, and more rapid disappearance of the signal, which are consistent with the lower average electron energies expected at higher pressure. Imaging results among the various gas mixtures tested were confounded by changes in the collisional quenching rates of the targeted excited states, among other factors.

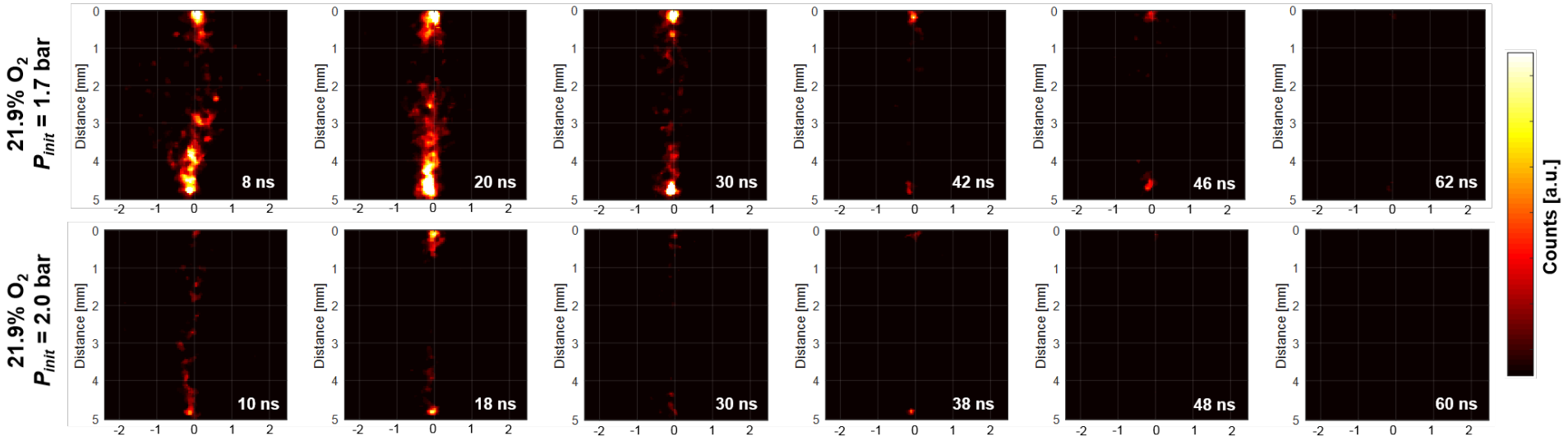

Figure 9. Electronically-excited O-atom images with a 5 ns gate duration for 18 kV_{peak} discharges in 21.9% O_2 at P_{init} = 1.7 bar (top row) and P_{init} = 2.0 bar (bottom row). Images are single-shot images from separate discharges with a 5x5 pixel spatial median filter applied for noise reduction. The start of image acquisition time relative to the start of the discharge is listed in the lower right corner of each image. Note that the horizontal dimension is the same as the vertical dimension and that the anode was located at (0,0).

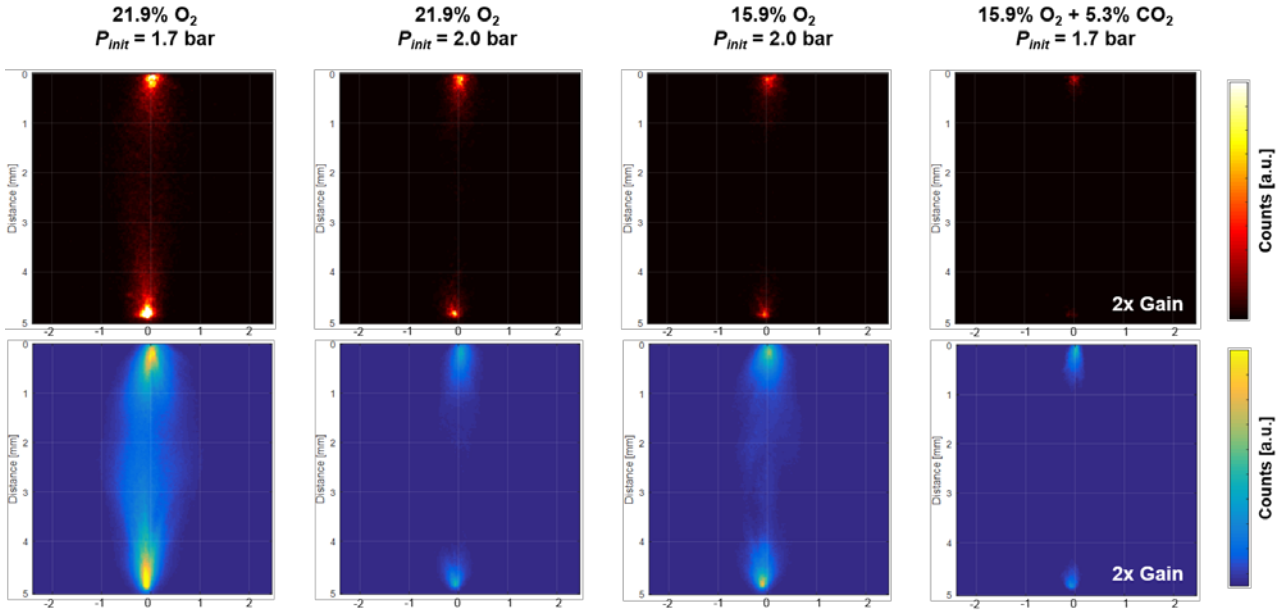

Figure 11. Median 500-ns gate images from electronically-excited O-atom (top) and broadband electronically-excited N_2 (bottom). Note that the horizontal dimension is the same as the vertical dimension and that the anode was located at (0,0).

Summary and Conclusions

In the current study, PND were evaluated in an optically accessible chamber using pressure-rise calorimetry and direct imaging. The impact of variations in O_2, CO_2, and H_2O mole fractions were evaluated for initial pressures up to 9 bar at 70°C for the calorimetry and 2 bar and 21°C for the imaging. The major findings of the study are:

- Two types of SSB discharges were observed: (Type 1) breakdown occurs shortly after the rising edge of the pulse before the pulse is reflected, and (Type 2) breakdown occurs during the damped, oscillating pulse reflections.
- The SSB occurrence probability, pulse electrical energy, and electrical-to-thermal energy conversion efficiency were found to not depend appreciably on O_2 or CO_2 concentration within the limits encountered in typical engine operation (0 to ~23% EGR). However, the addition of H_2O to the gas mixture had two measureable effects: (1) reduction of the pulse electrical energy for SSB Type 2 discharges by delaying the breakdown event further from the start of voltage rise, and (2) reduction of the electrical-to-thermal energy conversion efficiency for LTP discharges at $P_{init} < 7$ bar.
- Compared to a 5 mm gap, an Anode-only configuration had similar pulse electrical energy and electrical-to-thermal energy conversion efficiency. The Anode-only configuration reduced SSB probability from ~30% for a 5 mm gap to zero at an initial pressure of 4.0 bar, illustrating the main advantage of removing the cathode.
- Excited-state O-atom production was concentrated near the anode and cathode, which indicated that the presence of a cathode may be beneficial for increasing radical production compared to an anode-only configuration. Additionally, the observed signal near the cathode implied that the primary streamer led to substantial O-atom production, contrary to a previous description in the literature. Increasing initial pressure resulted in decreased excited-state O-atom signal, thinner structures, and more rapid disappearance of the signal.
- The observed intensities of the excited state O-atom and N_2 images were found to vary with initial pressure and gas composition. The importance of collisional quenching effects varied by gas mixture composition, for which the EEDF remained relatively unchanged.

A point-to-point electrode configuration was shown to be beneficial for maximizing radical production in PND, compared to an anode-only configuration. There is also potential to further improve PND ignition systems if breakdown during the oscillating, reflected pulse can be mitigated, such that higher peak voltages can be achieved in the initial pulse. The impact of the presence of fuel components will be evaluated in a future study.

References

1. Dale JD, Checkel MD, Smy PR, "Application of high energy ignition systems to engines," *Progress in Energy and Combustion Science*, 23 (5-6):379-98, 1997, doi: 10.1016/S0360-1285(97)00011-7.
2. Sun WT, Uddi M, Won SH, Ombrello T, Carter C, Ju YG, "Kinetic effects of non-equilibrium plasma-assisted methane oxidation on diffusion flame extinction limits," *Combustion and Flame*, 159 (1):221-9, 2012, doi: 10.1016/j.combustflame.2011.07.008.
3. Wolk B, DeFilippo A, Chen JY, Dibble R, Nishiyama A, Ikeda Y, "Enhancement of flame development by microwave-assisted spark ignition in constant volume combustion chamber," *Combustion and Flame*, 160 (7):1225-34, 2013, doi: 10.1016/j.combustflame.2013.02.004.
4. Mintusov E, Serdyuchenko A, Choi I, Lempert WR, Adamovich IV, "Mechanism of plasma assisted oxidation and ignition of ethylene-air flows by a repetitively pulsed nanosecond discharge," *Proceedings of the Combustion Institute*, 32:3181-8, 2009, doi: 10.1016/j.proci.2008.05.064.
5. Kosarev IN, Aleksandrov NL, Kindysheva SV, Starikovskaia SM, Starikovskii AY, "Kinetics of ignition of saturated hydrocarbons by nonequilibrium plasma: CH4-containing mixtures," *Combustion and Flame*, 154 (3):569-86, 2008, doi: 10.1016/j.combustflame.2008.03.007.
6. Jaggers HC, von Engel A, "Effect of Electric Fields on Burning Velocity of Various Flames," *Combustion and Flame*, 16 (3):275-&, 1971, doi: 10.1016/S0010-2180(71)80098-6.
7. Leonov SB, Yarantsev DA, "Plasma-induced ignition and plasma-assisted combustion in high-speed flow," *Plasma Sources Science & Technology*, 16 (1):132-8, 2007, doi: 10.1088/0963-0252/16/1/018.
8. Ju YG, Lefkowitz JK, Reuter CB, Won SH, Yang XL, Yang S, et al., "Plasma Assisted Low Temperature Combustion," *Plasma Chemistry and Plasma Processing*, 36 (1):85-105, 2016, doi: 10.1007/s11090-015-9657-2.
9. Ju YG, Sun WT, "Plasma assisted combustion: Progress, challenges, and opportunities," *Combustion and Flame*, 162 (3):529-32, 2015, doi: 10.1016/j.combustflame.2015.01.017.
10. Nishiyama A, Ikeda Y, "Improvement of Lean Limit and Fuel Consumption Using Microwave Plasma Ignition Technology," SAE International 2012-01-1139, 2012, doi: 10.4271/2012-01-1139.
11. Wang Q, Zhang G, Liu Y, Hou L, Liu C, Microwave plasma ignition process of methane and air mixture under high pressure. Proc Pulsed Power Conference (PPC), 2013 19th IEEE, 16-21 June 2013, 2013, p. 1-3.
12. Michael JB, Chng TL, Miles RB, "Sustained propagation of ultra-lean methane/air flames with pulsed microwave energy deposition," *Combustion and Flame*, 160 (4):796-807, 2013, doi: 10.1016/j.combustflame.2012.12.006.
13. Ju Y, Sun W, "Plasma assisted combustion: Dynamics and chemistry," *Progress in Energy and Combustion Science*, 48:21-83, 2015, doi: http://dx.doi.org/10.1016/j.pecs.2014.12.002.
14. Chintala N, Bao AN, Lou GF, Adamovich IV, "Measurements of combustion efficiency in nonequilibrium RF plasma-ignited flows," *Combustion and Flame*, 144 (4):744-56, 2006, doi: 10.1016/j.combustflame.2005.08.040.
15. Pertl FA, Smith JE, "High-Level Modeling of an RF Pulsed Quarter Wave Coaxial Resonator with Potential use as an SI Engine Ignition Source," SAE International 2008-01-0089, 2008, doi: 10.4271/2008-01-0089.
16. Hampe C, Kubach H, Spicher U, Rixecker G, Bohne S, "Investigations of Ignition Processes Using High Frequency Ignition," SAE International 2013-01-1633, 2013, doi: 10.4271/2013-01-1633.
17. Mariani A, Foucher F, Moreau B, "The Effects of a Radio Frequency Ignition System on the Efficiency and the Exhaust Emissions of a Spark-Ignition Engine," SAE International 2013-24-0053, 2013, doi: 10.4271/2013-24-0053.
18. Bozhenkov SA, Starikovskaia SM, Starikovskii AY, "Nanosecond gas discharge ignition of H-2- and CH4-

containing mixtures," *Combustion and Flame*, 133 (1-2):133-46, 2003, doi: 10.1016/S0010-2180(02)00564-3.
19. Kosarev IN, Aleksandrov NL, Kindysheva SV, Starikovskaia SM, Starikovskii AY, "Kinetic mechanism of plasma-assisted ignition of hydrocarbons," *Journal of Physics D-Applied Physics*, 41 (3) 2008, doi: 10.1088/0022-3727/41/3/032002.
20. Adamovich IV, Choi I, Jiang N, Kim JH, Keshav S, Lempert WR, et al., "Plasma assisted ignition and high-speed flow control: non-thermal and thermal effects," *Plasma Sources Science & Technology*, 18 (3) 2009, doi: 10.1088/0963-0252/18/3/034018.
21. Won SH, Jiang B, Dievart P, Sohn CH, Ju YG, "Self-sustaining n-heptane cool diffusion flames activated by ozone," *Proceedings of the Combustion Institute*, 35:881-8, 2015, doi: 10.1016/j.proci.2014.05.021.
22. Sevik J, Wallner T, Pamminger M, Scarcelli R, Singleton D, Sanders J, "Extending Lean and Egr-Dilute Operating Limits of a Modern Gdi Engine Using a Low-Energy Transient Plasma Ignition System," *Proceedings of the Asme Internal Combustion Engine Division Fall Technical Conference, 2015, Vol 1*, 2016.
23. Sjöberg M, Zeng W, Singleton D, Sanders JM, Gundersen MA, "Combined Effects of Multi-Pulse Transient Plasma Ignition and Intake Heating on Lean Limits of Well-Mixed E85 DISI Engine Operation," *SAE Int. J. Engines*, 7 (4):1781-801, 2014, doi: 10.4271/2014-01-2615.
24. Breden D, Raja LL, Idicheria CA, Najt PM, Mahadevan S, "A numerical study of high-pressure non-equilibrium streamers for combustion ignition application," *Journal of Applied Physics*, 114 (8) 2013, doi: 10.1063/1.4818319.
25. Shiraishi T, Urushihara T, Gundersen M, "A trial of ignition innovation of gasoline engine by nanosecond pulsed low temperature plasma ignition," *Journal of Physics D-Applied Physics*, 42 (13) 2009, doi: 10.1088/0022-3727/42/13/135208.
26. Starikovskiy A, Aleksandrov N, "Plasma-assisted ignition and combustion," *Progress in Energy and Combustion Science*, 39 (1):61-110, 2013, doi: http://dx.doi.org/10.1016/j.pecs.2012.05.003.
27. Scarcelli R, Sevik J, Wallner T, Richards K, Pomraning E, Senecal PK, "Capturing Cyclic Variability in Egr Dilute Si Combustion Using Multi-Cycle Rans," *Proceedings of the Asme Internal Combustion Engine Division Fall Technical Conference, 2015, Vol 2*, 2016.
28. Bastien F, Marode E, "Breakdown Simulation of Electronegative Gases in Non-Uniform Field," *Journal of Physics D-Applied Physics*, 18 (3):377-93, 1985, doi: 10.1088/0022-3727/18/3/007.
29. Ono R, Oda T, "Formation and structure of primary and secondary streamers in positive pulsed corona discharge - effect of oxygen concentration and applied voltage," *Journal of Physics D-Applied Physics*, 36 (16):1952-8, 2003, doi: 10.1088/0022-3727/36/16/306.
30. Teets RE, Sell JA, "Calorimetry of Ignition Sparks," SAE International 1988, doi: 10.4271/880204.
31. Gibalov VI, Pietsch GJ, "The development of dielectric barrier discharges in gas gaps and on surfaces," *Journal of Physics D-Applied Physics*, 33 (20):2618-36, 2000, doi: 10.1088/0022-3727/33/20/315.
32. Shiraishi T, Urushihara T, "Fundamental Analysis of Combustion Initiation Characteristics of Low Temperature Plasma Ignition for Internal Combustion Gasoline Engine," SAE International 2011-01-0660, 2011, doi: 10.4271/2011-01-0660.
33. Babaeva NY, Naidis GV, "On streamer dynamics in dense media," *Journal of Electrostatics*, 53 (2):123-33, 2001, doi: 10.1016/S0304-3886(01)00135-8.
34. Liu N, Pasko VP, "Effects of photoionization on similarity properties of streamers at various pressures in air," *Journal of Physics D-Applied Physics*, 39 (2):327-34, 2006, doi: 10.1088/0022-3727/39/2/013.
35. Lin YH, Singleton D, Sanders J, Kuthi A, Gundersen MA, Pressure effects on transient plasma discharge in air. Proc Pulsed Power Conference (PPC), 2013 19th IEEE, 16-21 June 2013, 2013, p. 1-5.
36. Tardiveau P, Marode E, Agneray A, Cheaib M, "Pressure effects on the development of an electric discharge in non-uniform fields," *Journal of Physics D-Applied Physics*, 34 (11):1690-6, 2001, doi: 10.1088/0022-3727/34/11/321.
37. Ono R, Nakagawa Y, Oda T, "Effect of pulse width on the production of radicals and excited species in a pulsed positive corona discharge," *Journal of Physics D-Applied Physics*, 44 (48) 2011, doi: 10.1088/0022-3727/44/48/485201.
38. van Veldhuizen EM, Rutgers WR, "Pulsed positive corona streamer propagation and branching," *Journal of Physics D-Applied Physics*, 35 (17):2169-79, 2002.
39. Nijdam S, Takahashi E, Markosyan AH, Ebert U, "Investigation of positive streamers by double-pulse experiments, effects of repetition rate and gas mixture," *Plasma Sources Science & Technology*, 23 (2) 2014, doi: 10.1088/0963-0252/23/2/025008.
40. Wolk B, Ekoto I, Calorimetry and Atomic Oxygen Planar Laser-Induced Fluorescence of Low-Temperature Plasma Discharges and Nanosecond Pulsed Discharges at Above-Atmospheric Pressures. Proc 3rd International Conference on Ignition Systems for Gasoline Engines, Berlin, Germany, 2016.
41. Niemi K, Schulz-von der Gathen V, Dobele HF, "Absolute atomic oxygen density measurements by two-photon absorption laser-induced fluorescence spectroscopy in an RF-excited atmospheric pressure plasma jet," *Plasma Sources Science & Technology*, 14 (2):375-86, 2005, doi: 10.1088/0963-0252/14/2/021.
42. Pancheshnyi SV, Starikovskaia SM, Starikovskii AY, "Collisional deactivation of N-2(C-3 Pi(u), v=0, 1, 2, 3) states by N-2, O-2, H-2 and H2O molecules," *Chemical Physics*, 262 (2-3):349-57, 2000, doi: Doi 10.1016/S0301-0104(00)00338-4.
43. Uddi M, Jiang NB, Mintusov E, Adamovich IK, Lempert WR, "Atomic oxygen measurements in air and air/fuel nano second-pulse. discharges by two photon laser induced fluorescence," *Proceedings of the Combustion Institute*, 32:929-36, 2009, doi: 10.1016/j.proci.2008.06.049.
44. Bittner J, Kohsehoinghaus K, Meier U, Just T, "Quenching of 2-Photon-Excited H(3s, 3d) and O(3p 3p2,1,0) Atoms by Rare-Gases and Small Molecules," *Chemical Physics Letters*, 143 (6):571-6, 1988, doi: Doi 10.1016/0009-2614(88)87068-4.
45. Albugues F, Birot A, Blanc D, Brunet H, Galy J, Millet P, et al., "Destruction of Levels C3iiu (V'=O, V'=1) of Nitrogen by O2,Co2,Ch4, and H2o," *Journal of Chemical Physics*, 61 (7):2695-9, 1974, doi: Doi 10.1063/1.1682401.
46. , MATLAB and Partial Differential Equation Toolbox, Release 2016a, The MathWorks, Inc., Natick, Massachusetts, United States.
47. Hagelaar GJM, Pitchford LC, "Solving the Boltzmann equation to obtain electron transport coefficients and rate coefficients for fluid models," *Plasma Sources Science & Technology*, 14 (4):722-33, 2005, doi: 10.1088/0963-0252/14/4/011.
48. Fridman A, "Plasma chemistry." Cambridge university press, 2008.

Contact Information

Benjamin Wolk
bmwolk@sandia.gov
Sandia National Laboratories
P.O. Box 969, MS 9053
Livermore, CA 94551, USA

Acknowledgments

This work was performed at the Combustion Research Facility, Sandia National Laboratories, Livermore, CA. Financial support was provided by the U.S. Department of Energy, Office of Vehicle Technologies. Sandia National Laboratories is a multi-mission laboratory managed and operated by Sandia Corporation, a wholly owned subsidiary of Lockheed Martin Corporation, for the U.S. Department of Energy's National Nuclear Security Administration under contract DE-AC04-94AL85000. The authors also gratefully acknowledge the engineering support provided by Alberto Garcia as well as the hardware support and fruitful technical discussions from Daniel Singleton and Jason Sanders of Transient Plasma Systems Inc. We further acknowledge technical engine data provided by Magnus Sjöberg of Sandia National Laboratories along with James Sevik, Riccardo Scarcelli, and Thomas Wallner of Argonne National Laboratory.

Definitions/Abbreviations

E	Electric field strength
E/N	Reduced electric field
EGR	Exhaust gas recirculation
I	Discharge current
IMEP	Indicated mean effective pressure
LTP	Low-temperature plasma
N	Number density
O	Atomic oxygen
PAI	Plasma-assisted ignition
PND	Pulsed nanosecond discharge
SSB	Secondary streamer breakdown
V	Discharge voltage
a	Fluorescence quantum yield
A	Spontaneous emission rate
c_v	Specific heat capacity (constant volume)
E_{elec}	Pulse electrical energy
E_{Therm}	Thermal energy deposited into gas
G	Intensifier gain
k_i	Quenching rate coefficient of species i
n_i	Number density of species i
P_{init}	Initial chamber pressure
Q	Quenching rate
R	Gas constant
t_p	Duration of pulse
V_{cal}	Calorimeter internal volume
W	Instantaneous discharge power
δu	Differential change in internal energy
ΔP	Differential pressure change